JOURNAL OF APPLIED ELECTROCHEMISTRY **26** (1996) 557–565

# Influence of rib spacing in proton-exchange membrane electrode assemblies

A. C. WEST

*Columbia University, Department of Chemical Engineering, Materials Science, and Mining Engineering, New York, NY 10027, USA*

T. F. FULLER

*International Fuel Cells, South Windsor, Connecticut 06074, USA*

Received 14 August 1995; revised 13 November 1995

A two-dimensional design analysis of a membrane-electrode assembly for a proton-exchange membrane fuel cell is presented. Specifically, the ribs of the bipolar plates restrict the access of fuel and oxidant gases to the catalyst layer. The expected change in cell performance that results from the partial blocking of the substrate layer is studied by numerical simulation of the oxygen electrode and the membrane separator. The effects of rib sizing and the thickness of the gas-diffusion electrode on the current and water distributions within the cell are presented. For all of the cases considered, the two-dimensional effect only slightly alters the half-cell potential for a given applied current but has a significant influence on water management.

Concentrated solution theory with variable transport properties is used in the membrane electrolyte to solve for the electrical potential and local water content. The Stefan–Maxwell equations are used in the gas-diffusion electrode to determine the local mole fractions of nitrogen, oxygen and water vapour.

A control-volume formulation is used for the resolution of the coupled nonlinear differential equations. One advantage of the control-volume approach over finite-difference methods is the relative ease in which internal boundary points in fuel-cell and battery models are handled. This and other advantages are briefly discussed.

## List of symbols

| | |
|---|---|
| $a$ | specific interfacial area ($m^{-1}$) |
| $A_k$ | kinetic parameter defined by Equation 19 ($kA\,m^{-2}$) |
| $c$ | concentration ($mol\,m^{-3}$) |
| $d_{ik}^e$ | coefficient in Equation 14 |
| $D$ | diffusion coefficient ($m^2\,s^{-1}$) |
| $f_{i,k}^e$ | coefficient in Equation 14 |
| $F$ | Faraday's constant (96 487 C equiv$^{-1}$) |
| $h$ | mesh spacing (m) |
| $i$ | current density in electrolyte ($A\,m^{-2}$) |
| $i_o$ | exchange current density ($A\,m^{-2}$) |
| $I$ | superficial current density ($A\,m^{-2}$) |
| $L_m$ | thickness of membrane (m) |
| $L_s$ | thickness of substrate (m) |
| $L_y$ | thickness of rib (m) |
| $M$ | molecular weight ($g\,mol^{-1}$) |
| $N_i$ | flux of species $i$ ($mol\,m^{-2}\,s^{-1}$) |
| $n$ | number of electrons transferred |
| $p$ | pressure (Pa) |
| $R$ | universal gas constant ($J\,mol^{-1}\,K^{-1}$) |
| $R_h$ | relative humidity |
| $R_i$ | reaction state of species $i$ ($mol\,m^{-3}\,s^{-1}$) |
| $s_i$ | stoichiometric coefficient |
| $T$ | temperature (K) |
| $V$ | cell potential (V) |
| $x$ | molar fraction of gas, and distance normal to membrane face (m) |
| $y$ | distance (m) |

*Greek symbols*

| | |
|---|---|
| $\alpha$ | diffusion coefficient ($J\,mol^2\,m^{-1}\,s^{-1}$) |
| $\alpha_e$ | weighting factor |
| $\beta_e$ | weighting factor |
| $\Delta x$ | element size in $x$-direction (m) |
| $\Delta y$ | element size in $y$-direction (m) |
| $\Phi$ | potential of electrolyte (V) |
| $\epsilon$ | porosity or numerical error |
| $\kappa$ | conductivity of electrolyte ($S\,m^{-1}$) |
| $\lambda$ | dimensionless water concentration in membrane (moles water/mole sulfonate group) |
| $\rho$ | membrane density ($kg\,m^{-3}$) |
| $\sigma_{AB}$ | characteristic length (m) |
| $\omega_0$ | mass fraction of water |
| $\Omega_{AB}$ | diffusion collision integral |
| $\xi$ | transport number of water |
| $\mu$ | chemical potential, $J\,mol^{-1}$ |

*Subscripts*

| | |
|---|---|
| e | east face |

eff effective transport property
m membrane
s substrate

*Superscripts*
e east face
* reference pressure (bar)

## 1. Introduction

The design of flow fields for fuel and oxidant feeds of a proton-exchange membrane (PEM) fuel cell is considered. The ribs of the bipolar plates restrict the access of fuel and oxidant gases to the catalyst layer, affecting the current distribution in the cell. The expected change in cell performance that results from the partial blocking of the substrate layer is an important factor in the design of a fuel-cell system. The sizing of the ribs and the thickness of the substrate also affect water distribution within a PEM cell. Perfluorinated ionomer membranes require absorbed water to maintain sufficient electrical conductivity for practical use, and it is vital to manage the water content in the solid-polymer electrolyte. From the inception of solid–polymer–electrolyte fuel cells, water transport was recognized as a problem. Water motion is caused by the movement of hydrogen ions, which is proportional to the current. High current densities can result in the transport of water away from the anode–membrane interface at a rate that is greater than the rate at which it can be restored by diffusion, or transported from a humidified gas stream.

Modelling is an important tool in the design and optimization of batteries and fuel cells. The numerical solution to the coupled, nonlinear, partial differential equations is usually carried out by means of a finite-difference formulation, using a block, tridiagonal matrix algorithm (TDMA), normally based on the Thomas method. For the numerical simulation of fuel cells and batteries, there are two shortcomings associated with the standard, Taylor series-based finite-difference approach.

First, inherent in any battery or fuel-cell system are interior boundaries separating distinct phases. For example, the interface between the electrolyte and the gas-diffusion electrode of a fuel cell forms a boundary for the gas and electrolyte phases, for which interior boundary conditions must be imposed. The standard finite-difference formulation of these interior boundary conditions results in block pentadiagonal matrices, which are more difficult to resolve than the tridiagonal matrices. Various schemes, including the employment of pentadiagonal matrix solvers, have been used to circumvent this problem [1, 2]. An alternative is to use derivatives whose accuracy is only first order in the node spacing. Although this allows internal boundaries to be readily handled, the low accuracy of this method may give unsatisfactory convergence results.

Second, the standard finite-difference method does not rigorously conserve material (or momentum and energy). The amount of electrolyte in a battery, for instance, may increase with simulation time, clearly a nonphysical result. The control-volume formulation, sometimes called the finite-volume method, rigorously conserves material and handles easily interior boundaries. These two advantages of the control-volume approach will become even more important as two or three-dimensional numerical simulations become prevalent.

The objectives of this paper are to review the control-volume formulation and to apply it to a two-dimensional problem of interest for fuel-cell modelling.

## 2. Control-volume formulation

The control-volume approach has been used extensively in heat-transfer and fluid-flow simulations [3], but to a lesser degree in the modelling of battery and fuel-cell systems. Recently, Fiard and Herbin [4] compared a control-volume approach to a finite-element method for the simulation of a solid–oxide fuel cell. They found that the control-volume technique was computationally superior to the finite-element approach and somewhat easier to implement. The control-volume method, or integrated element approach, has been used in conjunction with the finite-difference method to handle interior boundaries in fuel-cell [5] and battery modelling [6]. However, it is more logical to use the control-volume approach across the entire solution domain, as was done by Pollard and Newman [7, 8]. The benefits and details of their approach are not given in their paper.

The control-volume concept is simple – the differential form of the material balance is replaced with an integrated form. Consider one-dimensional transport in the element shown in Fig. 1. At steady state, a shell mass balance is written as

$$\left\{\begin{matrix}\text{rate of}\\ \text{mass in}\end{matrix}\right\} - \left\{\begin{matrix}\text{rate of}\\ \text{mass out}\end{matrix}\right\} + \left\{\begin{matrix}\text{rate of}\\ \text{production}\end{matrix}\right\} = 0$$

or on a unit area basis,

$$N_A\left(x-\frac{h}{2}\right) - N_A\left(x+\frac{h}{2}\right) + R_A h = 0 \qquad (1)$$

$N_A$ is the flux of species A, $R_A$ is the homogenous production rate, and $h$ is the thickness of the element. Typically, after making the balance for a shell of finite

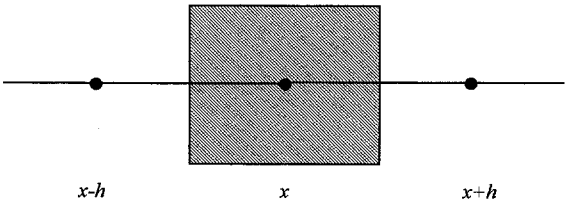


Fig. 1. A control volume used in the integrated-element approach. Fluxes are evaluated at the faces between node points. In this approach, material is rigorously conserved.

thickness, one lets the thickness of the shell, $h$, become infinitesimally small. Performing this and substituting Fick's law for diffusion gives

$$\frac{\mathrm{d}}{\mathrm{d}x}\left(D_{\mathrm{A}}\frac{\mathrm{d}c_{\mathrm{A}}}{\mathrm{d}x}\right)+R_{\mathrm{A}}=0 \qquad (2)$$

Equation 2 is then cast in finite-difference form via a Taylor-series expansion, and the resulting algebraic equations are solved numerically.

For the control-volume approach, the step letting the size of the shell become infinitesimally small is omitted, and one works directly with Equation 1. The fluxes at $x\pm\frac{1}{2}h$ are expressed with Fick's law and cast in finite difference form. In the limit of infinitesimally small $h$, the two methods give identical results.

One of the more attractive features of the control-volume formulation is the integral conservation of material, momentum etc. Since the fluxes in the common face between two adjacent control volumes are represented by the same expression, material is rigorously conserved. This conservation is preserved regardless of the mesh size. In contrast, it can be shown that, when $D_{\mathrm{A}}$ is not constant, the standard finite-difference approximation of Equation 2 conserves material only in the limit of $h$ approaching zero [9]. We should note that the spacing between grid points may still need to be reduced to obtain numerically the desired solution accuracy.

The control-volume approach is demonstrated by a two-dimensional model of the cathode of a PEM fuel cell. This problem, which is outlined below, was chosen because it is a good illustration of the technique, is a relevant problem to the technology, and is conceptually easy to follow.

## 3. Model

Figure 2 depicts the proton-exchange membrane, substrate, and flow fields for a typical PEM membrane and electrode assembly. In recent years, a number of models of PEM fuel cells have been presented [5, 10, 11]. As a consequence, we will give only the salient features of the physical model and concentrate on the control-volume formulation and the two-dimensional results.

Humidified air or oxygen flows through the gas channels (the white space at $x = L_{\mathrm{m}} + L_{\mathrm{s}}$). Between the bipolar plate and the catalyst layer, a porous substrate made from carbon cloth or carbon paper is placed. A ribbed structure is used for the flow fields. These plates serve to provide an electronic connection between the substrate and the adjacent cells in the bipolar design and to direct the flow of gases. Because of these ribs (the hatched region), access to a portion of the substrate is blocked. Oxygen must diffuse across the substrate to the interface between the membrane and substrate, where the platinum catalyst is located. Oxygen is reduced here to form water. This product water vapour must counter-diffuse out through the substrate and into the gas channels. The nitrogen is stagnant at steady state.

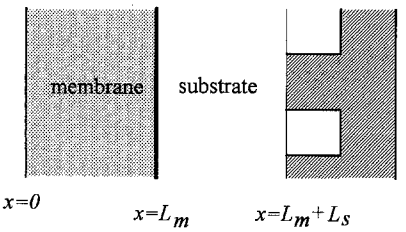


Fig. 2. Schematic of the regions of the positive electrode that are modelled. The substrate is porous carbon through which gases diffuse, the membrane is a polymer electrolyte with transference number of one, and oxygen reduction occurs at the catalyst layer $x = L_{\mathrm{m}}$. Humidified air is fed through the (white) flow channels at $x = L_{\mathrm{m}} + L_{\mathrm{s}}$.

Within the membrane, hydrogen ions move from the anode to the cathode under an electric field. The hydrogen ions react with oxygen at the cathode catalyst. Water is transported in the membrane by concentration gradients and by the electroosmotic drag associated with proton movement. Since the catalyst layer is thin in PEM cells, it is assumed here to have zero thickness.

### 3.1. *Gas-phase diffusion in substrate*

For diffusion in the substrate, the Stefan–Maxwell equation for molecular diffusion is used:

$$\frac{\nabla p_i}{RT}=\sum_{j\neq i}^{m}\frac{p_iN_j-p_jN_i}{pD_{ij}} \qquad (3)$$

For $m$ gas species, there are $m-1$ independent equations of the form of Equation 3. A relationship among fluxes is required to completely define the gas phase transport problem; here the flux of nitrogen is set to zero. For a three component system, the Stefan–Maxwell equations can be inverted to give

$$N_{\mathrm{A}}=\frac{\dfrac{p}{RT}\left[\dfrac{D_{\mathrm{BC}}}{D_{\mathrm{AB}}}\dfrac{p_{\mathrm{A}}}{p_{\mathrm{C}}}\nabla p_{\mathrm{C}}-\nabla p_{\mathrm{A}}\right]}{\left\{\dfrac{D_{\mathrm{BC}}}{D_{\mathrm{AC}}}\dfrac{p_{\mathrm{A}}}{D_{\mathrm{AB}}}+\dfrac{p_{\mathrm{B}}}{D_{\mathrm{AB}}}+\dfrac{p_{\mathrm{C}}}{D_{\mathrm{AC}}}\right\}} \qquad (4)$$

$$N_{\mathrm{B}}=\frac{D_{\mathrm{BC}}p\nabla p_{\mathrm{C}}}{RTp_{\mathrm{C}}}-N_{\mathrm{A}}\frac{D_{\mathrm{BC}}}{D_{\mathrm{AC}}} \qquad (5)$$

and

$$N_{\mathrm{C}}=0 \qquad (6)$$

A represents oxygen, B water vapour and C nitrogen.

A material balance on species $i$ (where $i$ = A or B) gives

$$0=-\nabla\cdot N_i+R_i \qquad (7)$$

where $R_i$ is the rate of production of species $i$ per unit volume of electrode. The flux relationships (Equations 4–6) are substituted into Equations 7. The control-volume approach is used, evaluating the fluxes between mesh points (see Equation 1) using a central difference approximation for the gradients in partial pressure.

### 3.2. *Electrode kinetics*

In this analysis, the thickness of the catalyst layer is assumed to be zero and the homogeneous reaction rates are zero. The reduction of oxygen is adequately modelled with Tafel kinetics first order in oxygen pressure [12]. The flux of oxygen at the substrate/catalyst layer interface, given by Faraday's law, can then be related to the applied potential $V$ through the following equation:

$$N_{O_2}|_{x=L_m} = \frac{i}{nF} = \frac{i_o}{nF}\frac{p_{O_2}}{p^*_{O_2}}\exp\left\{\frac{-F}{RT}(V-\Phi)\right\} \quad (8)$$

where $V$ is the potential of the metal at the catalyst layer, and $\Phi$ is the potential in the membrane at the catalyst layer. In our example, at $x = L_m$ the current flows in the $x$ direction only. The fluxes of other gas species are assumed to be directly related to the current through the reaction stoichiometry:

$$4H^+ + O_2 + 4e^- \longrightarrow 2H_2O$$

At the interface between the membrane and the gas phase, we assume equilibrium absorption of water vapour [13].

### 3.3. *Membrane transport*

Transport in the proton exchange membrane is described with concentrated solution theory. The perfluorinated ionomer membrane of the PEM fuel cell is a binary electrolyte. If there is rapid equilibrium between species, one can assume that there are only three species in the treatment of transport. We consider these to be the polymer with covalently bonded sulfonic acid moieties, hydrogen ions, and water. Since the hydrogen ions are the only mobile charged species, electroneutrality requires its concentration to be constant. Thus, two variables can be used to model the transport in the membrane: the electric potential $\Phi$ and the chemical potential of water $\mu_{H_2O}$. The current density and flux of water are proportional to gradients of these variables [14]:

$$i = -\kappa\nabla\Phi - \frac{\kappa\xi}{F}\nabla\mu_{H_2O} \quad (9)$$

$$N_{H_2O} = \frac{-\kappa\xi}{F}\nabla\Phi - \left\{\alpha + \frac{\kappa\xi^2}{F^2}\right\}\nabla\mu_{H_2O} \quad (10)$$

where $\alpha$, a transport property of the membrane, relates the flux of water to its gradient in chemical potential when the current density is zero:

$$N_{H_2O} = -\alpha\nabla\mu_{H_2O} \text{ (when } i = 0) \quad (11)$$

A balance on water in the membrane and conservation of charge lead to

$$\nabla\cdot i = 0 \quad (12)$$

and

$$\nabla\cdot N_{H_2O} = 0 \quad (13)$$

The transport properties of the membrane, which depend on water concentration, were estimated from data in the literature. More details are given in the Appendix.

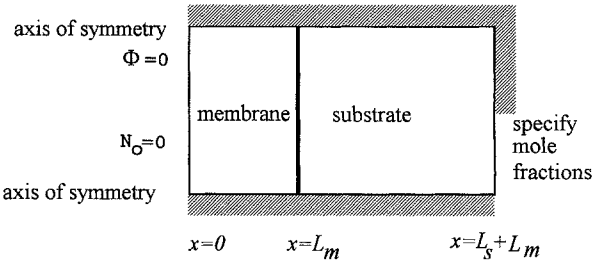


Fig. 3. The solution domain. The thick grey lines represent insulating boundary conditions.

### 3.4. *Boundary conditions*

The solution domain is shown in Fig. 3. On the two $y$ boundaries (the centre of the ribs and the centre of the gas channels), symmetry is assumed. Thus, zero flux conditions for all species are imposed. At $x = 0$, the flux of water is assumed to be a constant (zero for the results presented here), and the potential $\Phi$ is arbitrarily set equal to zero. If the negative electrode were also treated, the assumption of constant flux could be relaxed. This simplification was made to demonstrate the control-volume approach without introducing unnecessary complexity. At the interface between the substrate and the membrane, the flux of oxygen is related to the current density through Faraday's law. Since absorption and evaporation of water is allowed, the difference between the flux of water in the membrane and in the flux in the substrate are related to the current density through Faraday's law at this interface. At $x = L_m + L_s$, for $y > L_y/2$ zero-flux conditions are imposed, and for $y < L_y/2$ the feed is assumed to be humidified air at a total pressure $p = 10^5$ Pa with a specified relative humidity (assumed to be 90% in this paper).

### 3.5. *Numerical approach*

The conservation equations for oxygen, water (in the membrane and substrate) and current were discretized according to a control-volume formulation. In this approach, fluxes are specified at the element faces (between node points). The general, linearized flux expression for species $i$ at node point $j$ along the 'east face' (see Figs 1 and 4) can be written as

$$N_{i,e} = \sum_k d^e_{i,k}\left.\frac{\partial c_k}{\partial x}\right|_e + f^e_{i,k}c_k|_e \quad (14)$$

where the $k$th variable at the east face can be written as an average of its value at node points $j_x$ and $j_x + 1$:

$$c_k|_e \approx \alpha_e c_k(j_x+1) + (1-\alpha_e)c_k(j_x) \quad (15)$$

and the derivative is approximated by

$$\left.\frac{\partial c_k}{\partial x}\right|_e \approx \beta_e(c_k(j_x+1) - c_k(j_x)) \quad (16)$$

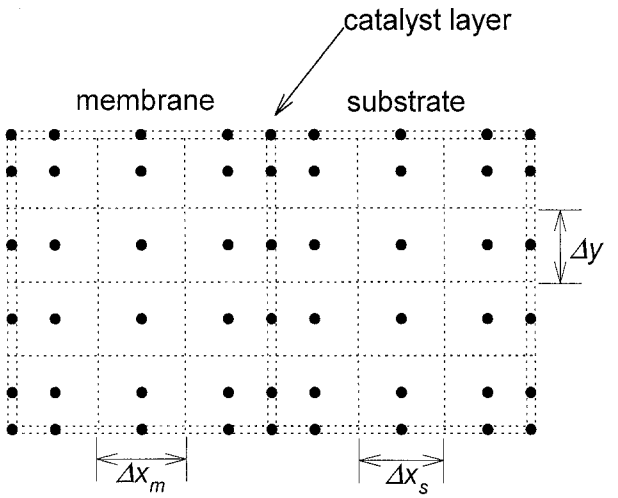


Fig. 4. An illustration of the two-dimensional mesh. At the boundaries, control volumes of zero thickness were used. In the membrane, the element size was $\Delta x_m \times \Delta y$, and in the substrate, $\Delta x_s \times \Delta y$.

The weighing factors $\alpha_e$ and $\beta_e$ are given by

$$\alpha_e = \frac{\Delta x_j}{\Delta x_j + \Delta x_{j+1}} \text{ and } \beta_e = \frac{2}{\Delta x_j + \Delta x_{j+1}} \quad (17)$$

For clarity, the subscripts $x$ have been omitted from Equation 17. Where the mesh size is uniform ($\Delta x_j = \Delta x_{j+1}$), $\alpha_e = 1/2$ and $\beta_e = 1/\Delta x_j$, and these equations are accurate to order $(\Delta x)^2$. As is indicated in Fig. 4, the 'zero-control volume method' was employed to take care of the boundaries and internal boundary ($x = L_m$). Equations 17 are still valid for the zero control volume, but the weighting values are different even for a uniform mesh size. In comparison with standard finite-difference methods, it appears as if 'half-mesh points' have been introduced to discretize derivative boundary conditions. Analogous relationships are written along the west, north, and south faces. For example, the equations for the north face are

$$N_{i,N} = \sum_k d^N_{i,k} \left.\frac{\partial c_k}{\partial y}\right|_N + f^N_{i,k} c_k|_N$$

$$c_k|_N \approx \alpha_N c_k(j_y + 1) + (1 - \alpha_N) c_k(j_y)$$

$$\left.\frac{\partial c_k}{\partial y}\right|_N \approx \beta_N (c_k(j_y + 1) - c_k(j_y))$$

$$\alpha_N = \frac{\Delta y_j}{\Delta y_j + \Delta y_{j+1}} \text{ and } \beta_N = \frac{2}{\Delta y_j + \Delta y_{j+1}}$$

The resulting set of coupled algebraic equations were solved with a standard line-by-line, successive over-relaxation procedure [3]. To solve for one line of variables, Newman's BAND and MATINV subroutines, a block TDMA, were used. Convergence of the two-dimensional solver was improved significantly by using an initial guess generated by the analogous one-dimensional problem, where at $x = L_m + L_s$ the mole fractions are everywhere specified to be the feed value. A relative convergence tolerance of $10^{-7}$ was used.

Figure 4 illustrates the mesh that was used. The size of the rectangular element in the substrate is $\Delta x_s \times \Delta y$ and is $\Delta x_m \times \Delta y$ in the membrane. The convention of placing the node point in the centre of the element (i.e., the region between dashed lines) was followed. An equal number of elements was used in the substrate and the membrane, thus $(\Delta x)_m = L_m/L_s(\Delta x)_s$. For all of the results reported below, the number of elements in the $y$ direction was set so that $(\Delta y) = 2L_m/L_s(\Delta x)_s$. For most of the results reported below, $(\Delta x)_s = 0.05\,L_s$, corresponding to a $43 \times 42$ mesh, was used. Node-point doubling was used to verify that results did not change appreciably.

### 3.6. *Model parameters*

Typical parameters are given in Table 1. The dimensions were taken from work of Wilson *et al.* [15] and are representative of typical values in PEM fuel cells. A more complete design of the bipolar plate and flow fields would also consider the pressure drop of the gases, structural integrity of the ribs, limits on machining, and the electronic resistance of the plates. For the results presented here, the ribs were assumed to cover half of the flow field, and the thickness of the substrate compared to the width of the rib was varied. Transport and kinetic data are summarized in the Appendix.

## 4. Results and discussion

To show that only one kinetic parameter influences the half-cell performance, Equation 8 for the flux in the $x$ direction at the catalyst layer can be written as

$$N_{O_2}|_{x=L_m} = \frac{A_k x_{O_2}}{nF} \exp\left\{\frac{F\Phi}{RT}\right\} \quad (18)$$

where

$$A_k = i_o \frac{p}{p^*_{O_2}} \exp\left\{\frac{-FV}{RT}\right\} \quad (19)$$

In Fig. 5, the influence of the kinetic parameter $A_k$ on the results of one-dimensional simulations is presented. The solid line gives the current density, and the dashed lines are the dimensionless water concentrations $\lambda$ at $x = 0$ and $x = L_m$, where $\lambda$ is the number of water molecules per sulfonic acid group. At low values of $A_k$, the current density is proportional to

*Table 1. Summary of dimensions and parameters used in the simulations*

| | |
|---|---|
| $A_k$ | varies |
| $L_s$ | 350 $\mu$m |
| $L_m$ | 50 $\mu$m |
| $L_y$ | between 300 and 1200 $\mu$m |
| $p$ | $10^5$ Pa |
| Relative humidity of feed | 90% |
| $T$ | 80° C |
| $\epsilon$ | 0.4 |

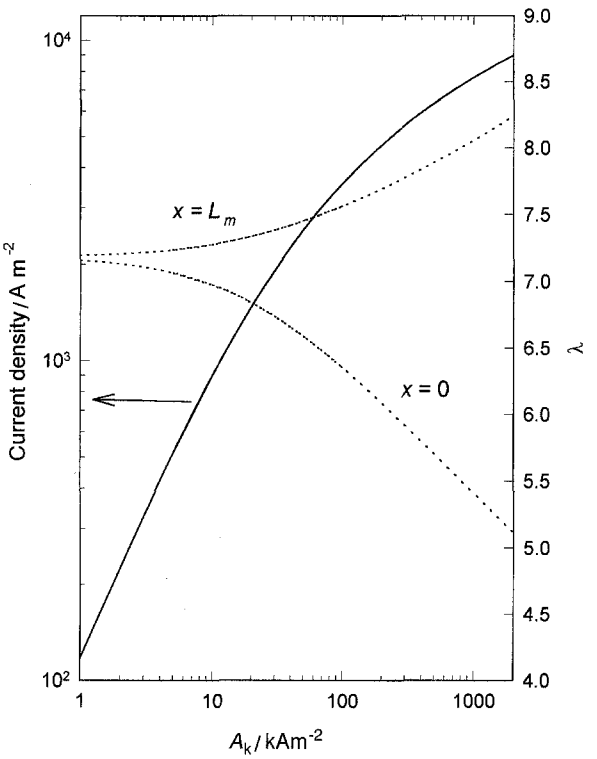


Fig. 5. Summary of one-dimensional simulations. The solid line gives the current density as a function of the kinetic parameter $A_k$. The dashed lines give the dimensionless water concentration at the two edges of the membrane.

$A_k$. At larger $A_k$, the transport limitations of the membrane and substrate reduce the current density. With the zero-flux boundary condition imposed at $x = 0$, a concentration gradient of water is established in the membrane to balance the elecroosmotic drag toward the cathode. At higher current densities, the anode side of the membrane dehydrates and the water content in the cathode side increases.

In Fig. 6, results of two-dimensional simulations are shown. Specifically, the dimensionless membrane-water concentration $\lambda$ at the catalyst layer ($x = L_m$) is given as a function of dimensionless distance $y/L_y$ for $A_k = 150\,\mathrm{kA\,m^{-2}}$. The variation in water concentration is shown for three geometric ratios. The water concentration reaches a maximum at the top of the cell (under the centre of the rib) because the water vapour must travel the longest distance from this point to exit into the flow field. For this simulation, the membrane is thin and the substrate thick. Consequently, the profile at $x = 0$ is nearly identical. Qualitatively similar water-concentrations profiles with a maximum at the top of the cell resulted from all simulations.

In Fig. 7, the current density at the catalyst layer ($x = L_m$) as a function of dimensionless distance $y/L_y$ for $A_k = 150\,\mathrm{kA\,m^{-2}}$ and $L_y/L_s = 3$ is represented by the open circles. That the maximum in current density appears at the top of the cell is perhaps surprising since the oxygen mole fraction $x_{O_2}$, shown by the bottom solid curve in Fig. 7, decreases with $y$. The explanation for this is that $\exp(F\Phi/RT)$ increases with increasing $y$. A decrease in ohmic potential drop near the top of the cell causes $\Phi$ to become less negative. This decrease in ohmic potential drop – despite an increase in current density in this region – arises because the membrane conductivity increases with increasing water concentration (see Equation 24).

The variations of $\lambda$, $x_{O_2}$, and $\exp(F\Phi/RT)$ with $y/L_y$ were qualitatively similar for all cases studied. Nevertheless, since $x_{O_2}$ decreases with $y$ and $\exp(F\Phi/RT)$ increases with $y$, the qualitative behaviour of the current density (see Equation 18) is more difficult to predict. In fact depending on the values of $A_k$ and $L_m/L_s$, simulations indicate that the maximum in

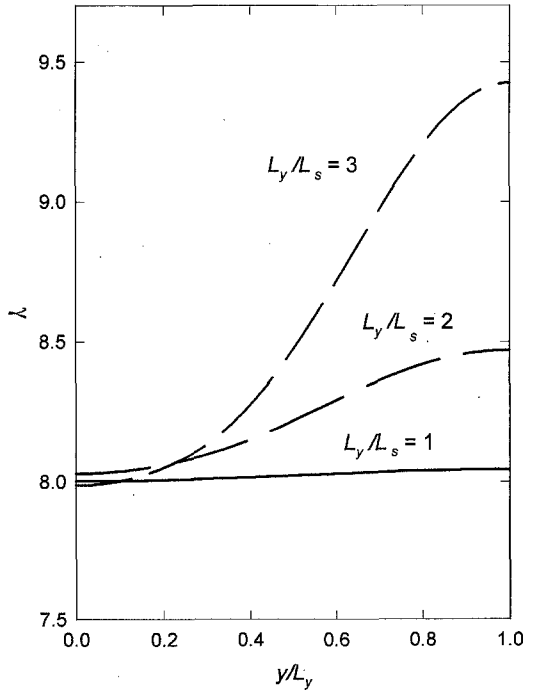


Fig. 6. The dimensionless water concentration at the catalyst layer ($x = L_m$) as a function of dimensionless distance for $A_k = 150\,\mathrm{kA\,m^{-2}}$ and three geometric ratios.

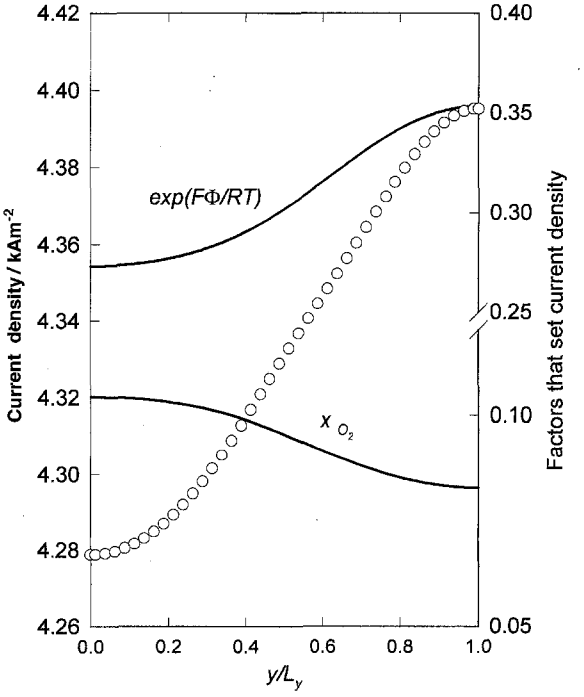


Fig. 7. The spatial variations of current density (the hollow points), mole fraction of oxygen, and electrical potential at the catalyst layer ($x = L_m$) for $A_k = 150\,\mathrm{kA\,m^{-2}}$ and $L_y/L_s = 3$.

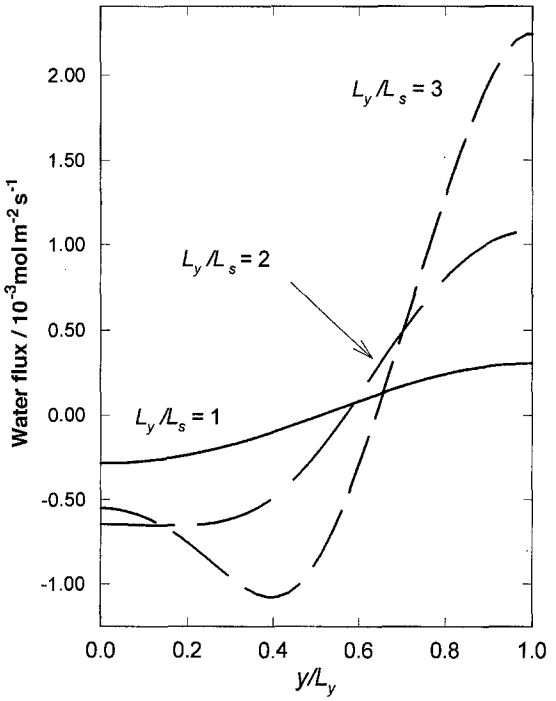


Fig. 8. The flux of water into the membrane as a function of position along the catalyst layer for $A_k = 150\,\mathrm{kA\,m^{-2}}$ and three geometric ratios. A positive flux represents water entering the membrane, and a negative flux corresponds to water exiting the membrane. The spatial average of the flux is zero.

current density can occur at any position along the catalyst layer. For all of the cases studied, the difference between the maximum and minimum current was less than twenty percent, and the difference between the spatial average of the current density and the current density resulting from the one-dimensional simulation was less than ten percent.

In a one-dimensional, steady simulation, conservation of mass requires that the water flux across the membrane be constant. Since a zero-flux condition is imposed at $x = 0$, the flux of water would everywhere be zero. This is not necessarily true in two-dimensions since water can exit and enter through different positions along the catalyst layer. This is illustrated in Fig. 8, which shows that water enters into the membrane near the top of the cell and exits near the bottom (at the centre of the flow fields). Of course, the net flux averaged over the catalyst layer remains zero. This effect is small and probably not of practical significance.

As mentioned above, simulations indicate that partial blocking of the substrate by the flow field will only have a minor impact on the half-cell performance (based on total current for a given $A_k$). It should be realized though that it is assumed in these simulations that there is no water condensation within the substrate. Since it is known that the existence of liquid water can have a major impact on fuel-cell performance, the two-dimensional effect may actually have a larger impact on the current-potential relationship than the simulations predict. At the least, as Fig. 9 indicates, the effect has important implications for water management, which is almost always a design consideration.

In Fig. 9, results of the two-dimensional simulations are summarized by the maximum in dimensionless water concentration (i.e., $\lambda$ at $y/L_y = 1$) along the catalyst layer as a function of $A_k$. Results for three geometric ratios are compared to the results of the one-dimensional simulations. The two filled points for $L_y/L_s = 4$ correspond to the use of an $83 \times 82$ grid (i.e., doubling of the node density).

According to the absorption data of Hinatsu *et al.* [13], when $\lambda$ exceeds around 9.2, water precipitation is expected. Thus, the one-dimensional simulation suggests that it is possible to operate at relatively large applied potentials (i.e., $A_k$) before condensation in the substrate occurs. For the ratio $L_y/L_s = 4$ for example, precipitation is expected at around $A_k = 65\,\mathrm{kA\,m^{-2}}$, corresponding to an average current density of around $3\,\mathrm{kA\,m^{-2}}$. For even larger geometric ratios, simulations predict water precipitation at still lower current densities.

The prediction of water precipitation within the substrate is in accord with actual behaviour. Nevertheless, once appreciable precipitation occurs, the present model should not be expected to provide quantitative agreement with a real system. The development of more realistic computer models for use in

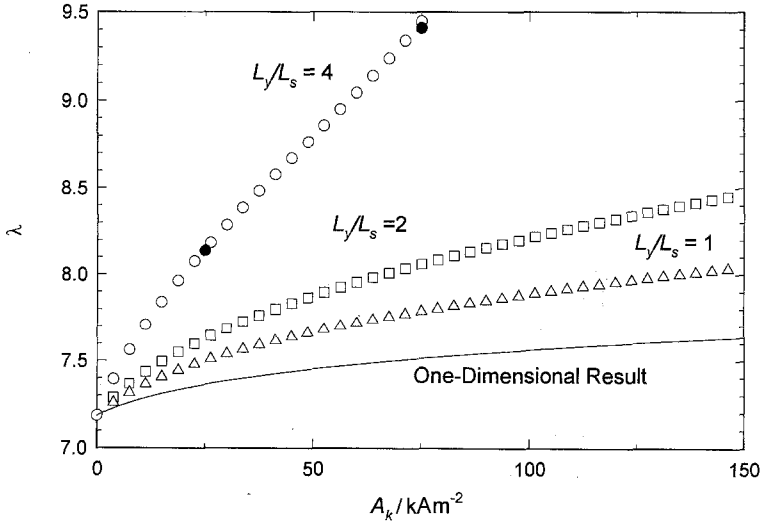


Fig. 9. The variation of the dimensionless water concentration at $x = L_m$ and $y = L_y$ with the kinetic parameter $A_k$ and three geometric ratios. For comparison, the predictions of a one-dimensional simulation are shown (the solid line).

fuel-cell optimization requires that water precipitation be included. In addition to modifying the governing transport equations in the substrate, the model should include information concerning how the membrane properties and the electrode kinetics change in the presence of liquid water.

## 5. Conclusions

The control-volume approach, applied here to a two-dimensional problem but also valid for one-dimensional studies, offers two advantages over the standard finite-difference formulation: it rigorously conserves material, and it facilitates the treatment of internal boundaries.

It is difficult to draw specific conclusions concerning the management of water in PEM fuel cells because thermal effects have not been treated, and the constant flux boundary condition imposed at $x = 0$ is a severe simplification, particularly for the two-dimensional simulation. Nonetheless, these results indicate that increasing the width of the ribs strongly affects the water content in the membrane well before the catalyst utilization is reduced because of oxygen diffusion resistance. For the positive electrode model presented, the resistance to the diffusion of product water from under the ribs caused the water content in the membrane to increase. Analogously, we should expect that the rib size of the negative electrode would have a strong effect on the hydration level of the membrane at the anode.

## References


[1] D. Fan and R. E. White, *J. Electrochem. Soc.* **138** (1991) 1688–91.

[2] J. Van Zee, G. Kleine, R. E. White and J. Newman, *in* 'Electrochemical Cell Design' (edited by R. E. White) Plenum Press, New York (1988), pp. 377–89.

[3] S. V. Patankar, 'Numerical Heat Transfer and Fluid Flow', McGraw-Hill, New York (1980).

[4] J. M. Fiard and R. Herbin, *Comput. Methods Appl. Mech. Eng.* **115** (1994) 315–38.

[5] T. F. Fuller and J. Newman, *J. Electrochem. Soc.* **140** (1993) 1218–25.

[6] M. Doyle, T. F. Fuller and J. Newman, *J. Electrochem. Soc.* **140** (1993) 1526–33.

[7] R. Pollard and J. Newman, *J. Electrochem. Soc.* **128** (1981) 491–502.

[8] R. Pollard, 'Mathematical Modeling of the Lithium–Aluminum, Iron Sulfide Battery', Dissertation, University of California, Berkeley (1979).

[9] Charles Hirsch, 'Numerical Computation of Internal and External Flows. Fundamentals of Numerical Discretization', John Wiley & Sons, New York (1988).

[10] D. M. Bernardi and M. W. Verbrugge, *J. Electrochem. Soc.* **139** (1992) 2477.

[11] T. E. Springer, T. A. Zawodzinski and S. Gottesfeld, *J. Electrochem. Soc.* **138** (1991) 2334–42.

[12] J. Newman, *Electrochim. Acta* **24** (1979) 223–9.

[13] J. T. Hinatsu, M. Mizuhata and H. Takenaka, *J. Electrochem. Soc.* **141** (1994) 1493–8.

[14] T. F. Fuller and J. Newman, *J. Electrochem. Soc.* **139** (1992) 1332–7.

[15] M. S. Wilson, J. A. Valerio and S. Gottesfeld, 'Endurance Testing of Low Pt Loading Polymer Electrolyte Fuel Cells', Abstract 607, 185th meeting of the Electrochemical Society, San Francisco, May (1994).

[16] R. B. Bird, W. E. Stewart and E. N. Lightfood, 'Transport Phenomena', John Wiley & Sons, New York (1960).

[17] T. F. Fuller, 'Solid-polymer-electrolyte Fuel Cells', PhD thesis, University of California, Berkeley, California (1992).


## Appendix

(a) *Transport properties in gas phase*

The diffusion coefficients in the gas phase were estimated from kinetic theory. Assuming the ideal-gas law holds, Bird *et al.* [16] give the approximate formula

$$D_{AB} = 1.8583 \times 10^{-5} \frac{\sqrt{T^3\left(\frac{1}{M_A} + \frac{1}{M_B}\right)}}{p\sigma_{AB}^2 \Omega_{AB}} \tag{20}$$

The effective transport properties for the gas phase were estimated using the Bruggemann relationship,

$$D_{eff} = D\epsilon^{1.5} \tag{21}$$

(b) *Transport properties in membrane*

Equations 9 and 10 can be replaced with [17]

$$i = -\kappa \nabla \Phi - \frac{\kappa \xi}{F} \frac{d\mu_{H_2O}}{d\lambda} \nabla \lambda \tag{22}$$

and

$$N_{H_2O} = \frac{-\kappa \xi}{F} \nabla \Phi - \left\{ \frac{\rho D_o}{(1 - \omega_o) M_{H_2O}} \frac{d\omega_o}{d\lambda} + \frac{\kappa \xi^2}{F^2} \frac{d\mu_{H_2O}}{d\lambda} \right\} \nabla \lambda \tag{23}$$

where $\rho$, $D_o$, $\omega_o$, $\kappa$ and $\xi$ all depend on the water content of the membrane $\lambda$. The following experimental data were used.

Springer *et al.* [11] measured the electrical conductivity of Nafion® 117 membranes at various temperatures and water contents.

$$\kappa = (0.005\,139\,\lambda - 0.003\,26) \times \exp\left\{1268\left(\frac{1}{303} - \frac{1}{T}\right)\right\} \tag{24}$$

The mutual diffusion coefficient is estimated by [17]

$$D_o = 3.5 \times 10^{-2} \exp\left\{\frac{-2436}{T}\right\} \frac{\lambda}{14} \tag{25}$$

The transport number of water is estimated with [17]

$$\xi = \left[\frac{1}{(0.35\lambda)^4} + \frac{1}{(1.47)^4}\right]^{-1/4} \tag{26}$$

The density of the membrane is assumed to be [17]

$$\rho = 10^3\left(\frac{1.98 + 0.0324\lambda}{1 + 0.0648\lambda}\right) \tag{27}$$

The mass fraction of water within the membrane is

given by

$$\omega_o = \frac{\lambda M_{H_2O}}{\lambda M_{H_2O} + EW} \quad (28)$$

where the equivalent weight of polymer, $EW$, is 1100.

(c) *Thermodynamic and kinetic data*

Equilibrium was assumed between the water vapour and the membrane at 80° C. The curve fit of Hinatsu *et al.* [13], for various membranes including Nafion® 117 and Nafion® 125 was used:

$$\lambda = 0.3 + 10.8\,R_h - 16.0R_h^2 + 14.1\,R_h^3 \quad (29)$$

where $R_h$ is the local relative humidity. By equating the relative humidity to gas-phase activity of water, a relationship between chemical potential and $\lambda$ was obtained and used for $d\mu_{H_2O}/d\lambda$ in Equations 22 and 23.